CHEMISTRY OF MATERIALS

ARTICLE

pubs.acs.org/cm

Single-Phase Dy_2O_3:Tb^{3+} Nanocrystals as Dual-Modal Contrast Agent for High Field Magnetic Resonance and Optical Imaging

Gautom Kumar Das,[†] Yan Zhang,[†] Loyola D'Silva,[§] Parasuraman Padmanabhan,[§] Boon Chin Heng,[||] Joachim Say Chye Loo,[||] Subramanian Tamil Selvan,[‡] Kishore K. Bhakoo,[§,*] and Timothy Thatt Yang Tan[†,*]

[†]Division of Chemical and Biomolecular Engineering, School of Chemical and Biomedical Engineering, Nanyang Technological University, 62 Nanyang Drive, Singapore 637459

[‡]Institute of Materials Research and Engineering, 3 Research Link, Singapore 117602

[§]Translational Molecular Imaging Group, Singapore Bioimaging Consortium, 11 Biopolis Way, Singapore 138667

[||]Division of Materials Science, School of Material Science and Engineering, Nanyang Technological University, Nanyang Avenue, Singapore 637459

Supporting Information

ABSTRACT: Ultrasmall terbium ions (Tb^{3+}) doped dysprosium oxide (Dy_2O_3) nanocrystals (NCs) of ~3 nm diameter have been synthesized and applied as a single-phase dual modality contrast agent for high field magnetic resonance imaging (MRI) and optical imaging. The NCs show excellent positive contrast at 7.0 T MRI in phantom and in vivo imaging in a mouse breast tumor model (MCF-7 cells) injected with NCs. In vitro confocal fluorescence microscopy images show the staining of cultured human bronchial epithelial cells (BEAS-2B) with green fluorescent NCs. In vitro cytotoxicity studies in BEAS-2B and L929 cells indicate that the bifunctional NCs have no appreciable toxicity at a concentration of up to 1000 μg/mL. These results suggest the potential application of these NCs as dual modality contrast agents in a combined high field MRI and fluorescence imaging.

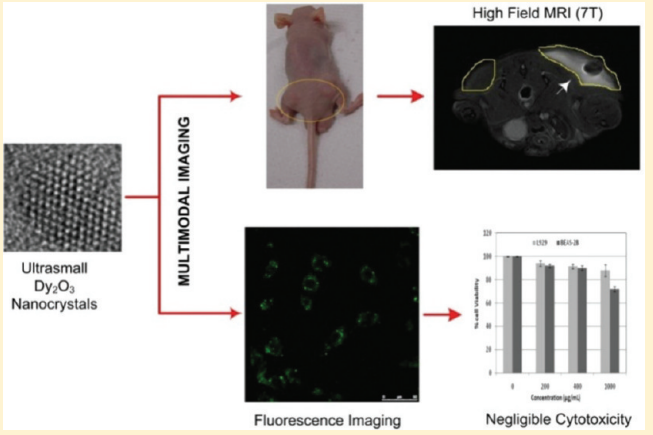

KEYWORDS: dysprosium oxide, high field MRI, T_2 contrast agents, fluorescent nanocrystals, multifunctional

1. INTRODUCTION

The complementary information obtained from multimodal imaging has led to increased accuracy of disease detection and diagnosis.[1−5] Two such complementary modalities are magnetic resonance imaging (MRI) and optical imaging. MRI is an important noninvasive tool in diagnostic clinical imaging that provides excellent opaque tissue contrast and spatial resolution.[5−7] Optical imaging is inexpensive, sensitive, and provides excellent temporal and spatial resolution, but depth penetration is limited to a few millimeters of tissue.[4] The fabrication of dual modality contrast agents may offer the combined advantages of MRI and optical imaging. Thus, in the past few years, nanomaterials with advanced magnetic or optical properties have been actively pursued for potential biological applications, including integrated imaging technologies applied to diagnosis and monitoring therapy.[3−5,8,9]

MR imaging relies on longitudinal (T_1) and transverse (T_2) relaxation times of endogenous water protons of the tissues to produce endogenous contrast. However, exogenous contrast agents can significantly alter the relaxation times and are used in MR imaging to provide both better contrast and functional information.[10] Most commonly, contrast agents are in the form of paramagnetic, superparamagnetic, or ferromagnetic reagents that shortens the relaxation times of bulk water protons.[7] Generally, T_1 contrast agents such as gadolinium(III) based chelates are used to shorten the longitudinal relaxation time (T_1) of surrounding water protons, which results in positive contrast. On the other hand, T_2 contrast agents, such as superparamagnetic iron oxide (SPIO) NCs, produce negative contrast by shortening transverse relaxation time (T_2) of surrounding water protons, thereby producing darker images.[7] However, SPIO NCs have been demonstrated to produce T_1-weighted positive contrast in a number of studies.[11−17] Chambon et al.[11] showed that at low concentrations (0.025−0.80 mM Fe), ultrasmall SPIO NCs (size 20 nm) produced good positive contrast at magnetic field strengths of 0.5−1.5 T. Cunningham et al.[13] reported 10−50 nm SPIO NCs as positive contrast agents by modulating the RF pulses during MR imaging.[13] Yet in another study, ultrasmall FeCo NCs (4−7 nm) have been reported as dual mode (exhibiting both T_1 and T_2) contrast agents.[17]

Received: January 30, 2011
Revised: March 24, 2011
Published: April 12, 2011

 © 2011 American Chemical Society

The present trend in clinical MRI is to move toward the use of higher magnetic field strength (3.0 T) to obtain a better signal-to-noise ratio.[6,18] For research and development of molecular imaging methods, even higher field MRI (>7 T) is promising due to enhanced resolutions, better defined chemical shifts spectra and larger data acquisition rates. However, at high magnetic fields, both paramagnetic T_1 contrast agents (such as the Gd^{3+}- based chelates) and superparamagnetic T_2 contrast agents (such as SPIO NCs) exhibit poor water relaxivity and low magnetization, as compared to those at low magnetic fields.[6,19,20] The Gd^{3+}-based contrast agents have longer electronic relaxation times due to their isotropic electronic ground state, which affects both T_1 and T_2.[21] Yet, most of the remaining paramagnetic lanthanide ions including Dy^{3+}, Pr^{3+}, Sm^{3+}, Ho^{3+}, Er^{3+}, and Yb^{3+} are characterized by shorter electronic relaxation time that mainly affects T_2.[22] Among them, Dy^{3+} has the shortest electronic relaxation time (~0.5 ps) and highest magnetic moment (10.6 μ_B) which result in very efficient T_2 relaxation.[21] Dy^{3+} ions induce proton relaxation via a Curie mechanism that primarily affects T_2. The contribution of Curie relaxation mechanism increases significantly with the external magnetic field, and is proportional to the square of the magnetic moment of the lanthanide ion.[23] These unique features of trivalent paramagnetic Dy^{3+} ions motivated us to choose Dy_2O_3 NCs in the current investigation as a potential contrast agent in high field MRI.

Dy^{3+}-based chelates have been studied previously and demonstrated their promise in T_2-weighted MRI.[6,21,23−25] However, Dy^{3+}-based T_2 contrast agents are fairly new in comparison with Gd^{3+}-based contrast agents that have been used widely over the years.[6,26−29] Among the earlier efforts, Bulte et al.[25] investigated Dy-DOTA-PAMAM dendrimers in magnetic field strengths ranging from 0.05 to 1.5 T, and reported its potential as contrast agent for high field MRI. Later, Elst et al.[23] examined a series of Dy-DTPA derivatives and demonstrated their potential as T_2 contrast agents in high field MRI (analyzed between 0.47 and 18.8 T). Recent studies have reported the synthesis of Dy_2O_3 NCs,[30,31] their physiochemical properties, NMR characterizations,[20] and investigation as contrast agents in high field MRI (analyzed from 7 to 17.6 T).[18]

In another aspect, trivalent lanthanide ion (Ln^{3+}) doping in nanoparticles have gained strong interest especially for the application as biolabels for fluorescent imaging because of their sharp emission spectra, high photostability, and nontoxicity.[32−36] Ln^{3+} doping in hosts such as fluorides, oxides, phosphates produce up- and down-conversion luminescence that arises from the intra 4f electron transitions of the doped lanthanide ion.[32] Significant research efforts have been made in the fabrication of Ln^{3+}-doped luminescent, and multifunctional nanocomposites to bridge the strengths of resolution and depth between MRI and optical imaging.[2,26,29,37−39] The majority of multifunctional nanoparticles have been fabricated by combining individual functionality via means of (i) core/shell formation,[40] (ii) heterodimer formation,[41] (iii) direct grafting of organic dyes on magneticnanoparticles,[42] and (iv) encapsulation of magnetic and fluorescent nanoparticles in silica or polymer shells.[43,44] In comparison, the notion of synthesizing single-phase multimodal NCs would be favorable in terms of ease of large-scale synthesis and functional homogenization.[45]

Herein, we report the synthesis of ultrasmall terbium-doped dysprosium oxide (Dy_2O_3:Tb^{3+}) NCs as a single-phase bimodal contrast agent using a simple synthetic strategy. To the best of our knowledge, this is the first report of Dy_2O_3 as a single-phase bimodal contrast agent that demonstrates the applicability of the NCs in high field MRI and optical imaging. The phantom images taken at 7.0 T MRI, and in vivo MRI images of a mouse model demonstrates that the ultrasmall Dy_2O_3:Tb^{3+} NCs (3 ± 0.4 nm) exhibit excellent positive contrast. Moreover, in vitro confocal fluorescent microscopy images of Dy_2O_3:Tb^{3+} NCs-loaded BEAS-2B cells showed that ultrasmall Tb^{3+}-doped Dy_2O_3 NCs were internalized by the cells and emitted green fluorescence, while in vitro cytotoxicity data suggest that the NCs present minimal toxicity. Most importantly, the current work demonstrates that Dy_2O_3:Tb^{3+} NCs are potential candidate as contrast agent for high field MRI, and also offer dual modality imaging, where MRI and fluorescence imaging can be allied to obtain information-rich images.

2. EXPERIMENTAL SECTION

Materials. Dysprosium(III) oxide (99.99%), terbium(III) chloride hexahydrate (99.9%), tetramethylammoniumhydroxide (25 wt % in methanol) (TMAH) and Igepal CO-520 (Polyoxyethylene(5)nonylphenylether), oleylamine (tech. 70%), were purchased from Aldrich. HNO_3 (analytical reagent, 70%), and oleic acid (tech. 90%) were purchased from Alfa Aesar. NaOH (reagent grade, 97%, beads), 3-aminopropyltrimethoxysilane (APS) (97%) were purchased from Fluka. Ethanol, hexane, cyclohexane, and chloroform were of analytical reagent grade. All chemicals were used as received without further purifications.

Synthesis of Tb^{3+}-Doped Dy_2O_3Nanocrystals (NCs). Typically, 0.95 mmol (0.3572 g) Dy_2O_3 and 0.05 mmol (0.0186 g) of $TbCl_3.6H_2O$ were dissolved in 0.4 mL HNO_3 (70%) and 1 mL H_2O. To this acidic solution, 5 mL H_2O, 12 mL ethanol, 18 mL hexane and 1 mL oleic acid were added in sequence. The mixture was then stirred in a closed vessel at 70 °C for 1 h. A second solution, prepared by dissolving 0.12 g NaOH in 2 mL H_2O was then added slowly and heated at 70 °C with stirring for another 4 h. After reaction, the mixture separated into two transparent layers. The organic layer containing the Dy−Tb-oleate complex was collected, washed with 30 mL of distilled water and dried overnight in an oven at 70 °C to evaporate water and hexane. The waxy Dy−Tb-oleate complex obtained after drying was dissolved in 12 mL oleylamine in a three-neck flask and purged with N_2. The solution was then heated to 280 °C at a rate of 5 °C/min under N_2 purging for 20 min. The mixture was then cooled to room temperature, precipitated by adding ethanol, and purified by centrifugation with extensive ethanol washing. The purified NCs were dispersed in cyclohexane for further characterizations.

Silanization of Tb^{3+}-Doped Dy_2O_3NCs. Silanization of the NCs was performed to render them water dispersible in a method described earlier.[46] Reverse micelles were prepared by dissolving 0.2 g of Igepal CO-520 in 4 mL of cyclohexane with vigorous stirring for 30 min. One ml of NCs (dispersed in chloroform at 10 mg/mL) were then added to the micelle solution and stirred for 15 min. Subsequently, 60 μL of APS was added and the mixture was stirred for another 1 h. Then, 60 μL of TMAH in methanol was added. After additional 1 h of stirring, 30 μL of deionized water was added and stirred for 30 min. At this stage, globules of silanized NCs were formed and settled at the bottom of the flask. The globules were then collected and the transparent organic phase was discarded. Silanized NCs were washed with chloroform and ethanol for the complete removal of excess surfactant and other reactants and finally dispersed in deionized water. The dispersed NCs were used for MRI and cytotoxicity studies.

Characterization of NCs. *Transmission Electron Microscopy.* The transmission electron microscopy (TEM) images and selected area electron diffraction (SAED) patterns were acquired using a JEOL JEM-2100F microscope operating at 200 kV. Two drops of

NCs dispersion was put onto a holey carbon film supported on a 200 mesh copper grid (3 mm in diameter) and allowed to dry in air at room temperature. The carbon grid with sample was then mounted into the vacuum chamber for imaging and SAED.

Powder X-ray Diffraction. Approximately 50 mg of the NCs sample was stirred gently in an agate mortar to break up lumps. The powdery samples were then spread evenly onto a zero-background holder. Step-scan X-ray powder diffraction data were collected over the range of 2θ range of 10−85° on a D8 Advance Bruker powder X-ray diffractometer with Cu Kα (operated at 40 kV, 40 kA) radiation ($\lambda = 0.15406$ nm) with 6 mm divergence slit, 1 mm scattering slit, and 0.2 mm receiving slit. The scanning step size was 0.015° 2θ with a counting time of 1 s per step.

Energy Dispersive X-ray Spectroscopy. Energy-dispersive X-ray (EDX) spectroscopy was done using a high resolution transmission electron microscope (JEOL, JEM 2100-F, Japan) operating at 200 kV and EDS (EDAX, AMETEK, U.S., system resolution: 135 eV). A few drops of NCs dispersion were put onto a holey carbon film supported on a 200 mesh copper grid (3 mm in diameter) and allowed to dry in air at room temperature. The carbon grid with sample was then mounted into the vacuum chamber for elemental compositional analysis.

Fluorescence Studies. NCs were dispersed in cyclohexane in a standard square quartz cuvette at room temperature and their photoluminescence spectra were obtained using a Shimadzu RF-5301 PC Spectrofluorometer fitted with a 150 W xenon lamp as the excitation source with a resolution of 1 nm.

Vibrating Sample Magnetometer (VSM). The magnetization values of the samples were acquired at room temperature with a LakeShore 7400 vibrating sample magnetometer (VSM) instrument using an applied magnetic field from 0 to 10 kOe. Approximately, 10 mg of dry powder samples were used for magnetization measurements.

Dynamic Light Scattering (DLS). The hydrodynamic size of the silanized NCs in aqueous suspension was measured by dynamic light scattering (DLS) experiments. DLS measurements were performed by a Brookhaven 90 Plus Particle Size Analyzer (Brookhaven Instruments Corporation) fitted with a 15 mW solid state laser.

Magnetic Resonance Imaging (MRI). *Phantom Studies.* The T_2-weighted images were obtained on a 7 T Bruker ClinScan MRI system. All samples were dissolved in double distilled water. The repetition time (TR) and echo time (TE) values were optimized for T_2-weighted imaging while using the spin echo sequence. Other parameters used for imaging are: number of acquisitions = 25, field of view = 35 mm, slice thickness = 2 mm, acquisition time ∼6 min/sample. All experiments were performed in 1% agarose medium.

In vivo Studies. In vivo studies were performed on a nude mouse injected with 5 million MCF-7 cells for induction of tumor. After 14 days of tumor growth (tumor size ∼0.5 mm) the contrast agent was injected directly into the tumor and imaged using the T_2-weighted spin echo sequence, with TR = 3s, TE = 38 ms, slice thickness = 1.0 mm, FOV = 40 mm.

Confocal Fluorescent Microscopy Imaging. BEAS-2B cells were seeded on glass coverslips within 6-well culture dishes at a density of 2.5×10^5 cells per well, and were subsequently exposed to 250 μg/mL of Tb^{3+}-doped Dy_2O_3NCs for a total duration of 24 h. After rinsing three times in PBS and fixation in 4% (w/v) paraformaldehyde (overnight at 4 °C), the cells on the coverslips were placed on glass slides and imaged under confocal fluorescent microscopy (LeicaTCS SP5; Leica Microsystems GmbH., Wetzlar, Germany) at an excitation wavelength of 405 nm and emission wavelength in the range of 500 to 560 nm, for qualitative assessment of NCs uptake by the cells.

Cytotoxicity Studies of Tb^{3+}-Doped Dy_2O_3 NCs. *Preparation of Monolayers of BEAS-2B and L929 Cells for Cytotoxicity Studies.* BEAS-2B and L929 cells were seeded on 12-well culture plates (≈ 4.8 cm^2 per well) at a density of 5.0×10^4 cells per well. The culture media was composed of Dulbecco's Minimum Essential Medium (DMEM) supplemented with 10% (v/v) fetal bovine serum (FBS) and 1% (v/v) antibiotic-antimycotic solution (Cat. No. A5955, Sigma-Aldrich Inc.). The seeded cells were then cultured for 24 h prior to being utilized for cytotoxicity assays.

Exposure of BEAS-2B and L929Cell Monolayers to Tb^{3+}-Doped Dy_2O_3 NCs. The following day after seeding, monolayers of BEAS-2B and L929 cells were exposed to varying concentrations (0, 200, 400, 1000 μg/mL) of Tb^{3+}-doped Dy_2O_3 NCs constituted in DMEM media (0.5 mL) supplemented with 10% (v/v) fetal bovine serum (FBS) and 1% (v/v) antibiotic-antimycotic solution (Cat No. A5955, Sigma-Aldrich Inc.), for a duration of 48 h at 37 °C within a 5% CO_2 incubator. Prior to incubation with either L929 or BEAS-2B cells, the NCs suspensions within culture media were sonicated for 30 min within an ultrasonic cleaner (MRC laboratory instruments Inc., Holon, Israel). Altogether, there were four replicates for each different NCs concentration within the experimental and control groups.

WST-8 Assay for Assessing Cell Viability upon Exposure to the Tb^{3+}-Doped Dy_2O_3 NCs. The cells were subjected to the WST-8 assay[47] after 48 h of exposure to varying concentrations of Dy_2O_3:Tb^{3+}NCs. The WST-8 assay for cell viability was carried out with the cell counting kit solution (CCK-8) from Dojindo Molecular Laboratories Inc. (Kumamoto, Japan). The CCK-8 kit utilizes the water-soluble tetrazolium salt WST-8 (2-(2-methoxy-4-nitrophenyl)-3-(4-nitrophenyl)-5-(2,4-disulfophenyl)-2H-tetrazolium, monosodium salt) in measuring NADH production resulting from the dehydrogenase activity of viable cells. The subsequent reduction of WST-8 by viable cells produces an orange-colored formazan product with an absorbance at 450 nm. The cells were washed three times in PBS (phosphate buffered saline), prior to the addition of 25 μL of CCK-8 solution and 225 μL of culture media within each well of the 12-well culture plate. After incubation for 1 h at 37 °C within a 5% CO_2 incubator, 100 μL aliquots of the reaction mixture were transferred onto a fresh 96-well plate, and absorbance readings were measured spectrophotometrically at 450 nm using an Infinite200 microplate reader (Tecan Inc., Maennedorf, Switzerland). The cell viability after exposure to varying concentrations of Dy_2O_3:Tb^{3+}NCs for 48 h, was calculated as the ratio of absorbance readings (450 nm) yielded by the treated and untreated (negative control) wells, after correction for blank absorbance reading of the reaction mixture incubated without cells for the same duration at 37 °C.

3. RESULTS AND DISCUSSION

The thermal decomposition of Tb−Dy-oleate complex at a fixed reaction temperature of 280 °C for 20 min resulted in uniform ultrasmall NCs. The TEM images of the Dy_2O_3:Tb^{3+}NCs are presented in Figure 1. Monodisperse spherical Dy_2O_3:Tb^{3+}NCs of average size 3.0 ± 0.4 nm were produced after refluxing the reaction mixture for 20 min (Figure 1a). Figure 1b shows HRTEM image of few NCs while the upper inset shows the lattice fringes of a nanocrystal. The interplanar distance was measured to be 0.30 nm, which corresponds to the (222) planes of cubic Dy_2O_3. The X-ray diffraction (XRD) pattern (Figure 2a) is consistent with the body-centered cubic

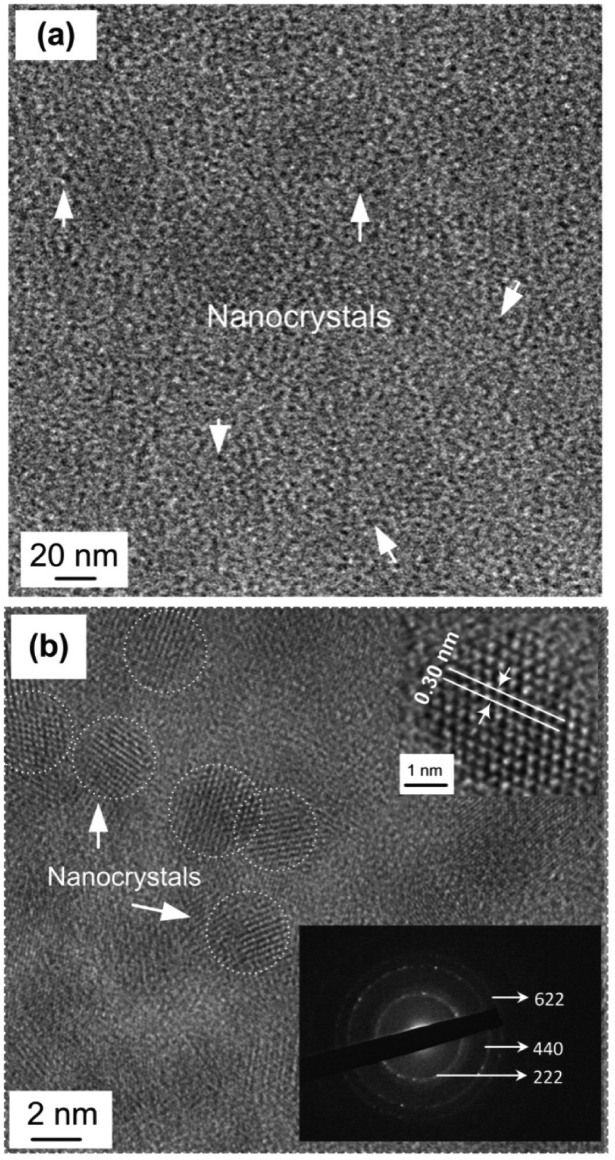

Figure 1. (a) TEM image of Dy_2O_3:Tb^{3+}NCs. (b) HRTEM image of few NCs highlighted by dotted circles; Upper inset: HRTEM of a single nanocrystal; Lower inset: Selected area electron diffraction (SAED) pattern of Dy_2O_3:Tb^{3+}NCs.

structure of dysprosium oxide (JCPDS File No. 00-022-0612). The wide diffraction peaks are consistent with nanocrystallite size, with Scherrer line-width analysis yielding a particle diameter of 2.8 nm, in agreement with TEM. Selected area electron diffraction (SAED) from NCs agglomerates (lower inset of Figure 1b) can be indexed as cubic Dy_2O_3 with (222), (440) and (622) diffraction rings at real space interplanar distances of 0.307, 0.188, and 0.160 nm, respectively. The hydrodynamic sizes of the silanized NCs in aqueous dispersion were measured by dynamic light scattering (DLS) technique (Figure S1 in the Supporting Information). The DLS data suggest that the NCs are well dispersed in aqueous dispersion with a narrow size distribution and a mean diameter of 7.0 nm. Energy dispersive X-ray (EDX) spectroscopy for Tb^{3+}-doped Dy_2O_3 is shown in Figure 2b. The analysis suggests that the concentration of Tb in Dy_2O_3:Tb^{3+} is 6.1 mol %. The C and Cu peaks are resulted

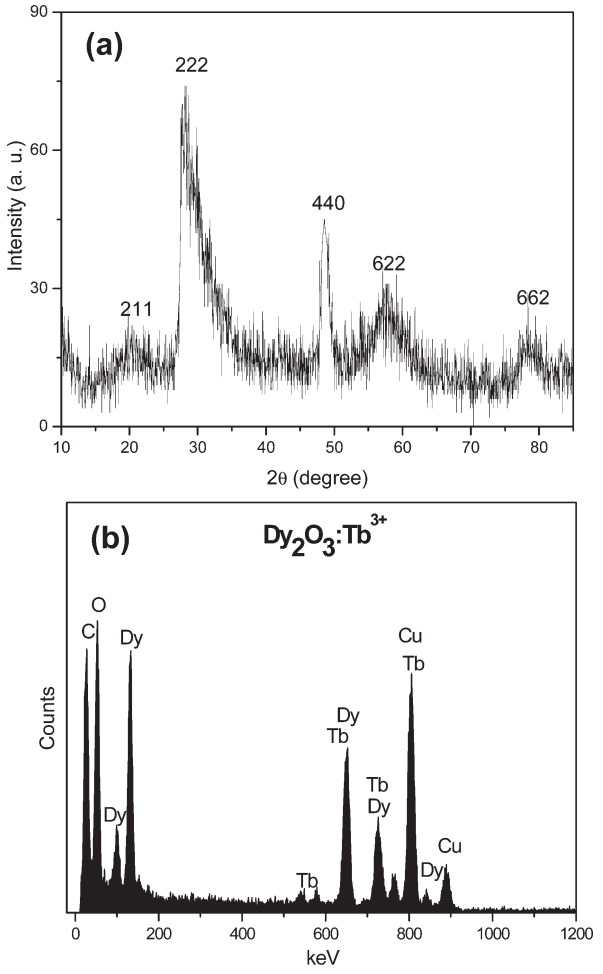

Figure 2. (a) XRD pattern, (b) energy dispersive X-ray (EDX) analysis of Dy_2O_3:Tb^{3+}NCs.

from the capping ligands, oleic acid/oleylamine and copper grid used for TEM, respectively.

The room temperature magnetization (M) as a function of applied field (H) (−10 to +10 kOe) for Tb^{3+}-doped and undoped Dy_2O_3NCs were investigated. Figure 3a shows a linear correlation (M vs H) with a magnetization value of 2.16 emu/g (at 10 kOe), suggesting that the Dy_2O_3:Tb^{3+} NCs are paramagnetic. Both Tb^{3+}-doped and undoped- Dy_2O_3NCs showed similar pattern and value of magnetization across the investigated field, indicating that very small amount of Tb^{3+} doping did not have an appreciable effect on the magnetization profile of the NCs. The transverse (T_2) relaxation times were measured at solutions of different Dy^{3+} ions concentrations (Figure 3b) at 7.0 T. The transverse relaxivity (r_2) was determined to be 2.17 $mM^{-1}s^{-1}$. The phantom images (Figure 4a) show a clear dose-dependent change in positive contrast due to increase in water proton relaxation with increasing dose. This is indicative of good sensitivity of the ultrasmall dysprosium oxide NCs in positive T_2-weighted MR imaging. Additionally, we used a nude mouse breast tumor model (MCF-7) to examine in vivo T_2-weighted MRI (Figure 4b) by injecting the contrast agents directly into the tumor. Figure 4c shows an image of the tumor on the flank region of the mice injected with the contrast agent dissolved in saline. The positive contrast arising from Dy_2O_3 NCs can be clearly seen at the injection site (right arrow) while

dx.doi.org/10.1021/cm2003066 |*Chem. Mater.* 2011, 23, 2439–2446

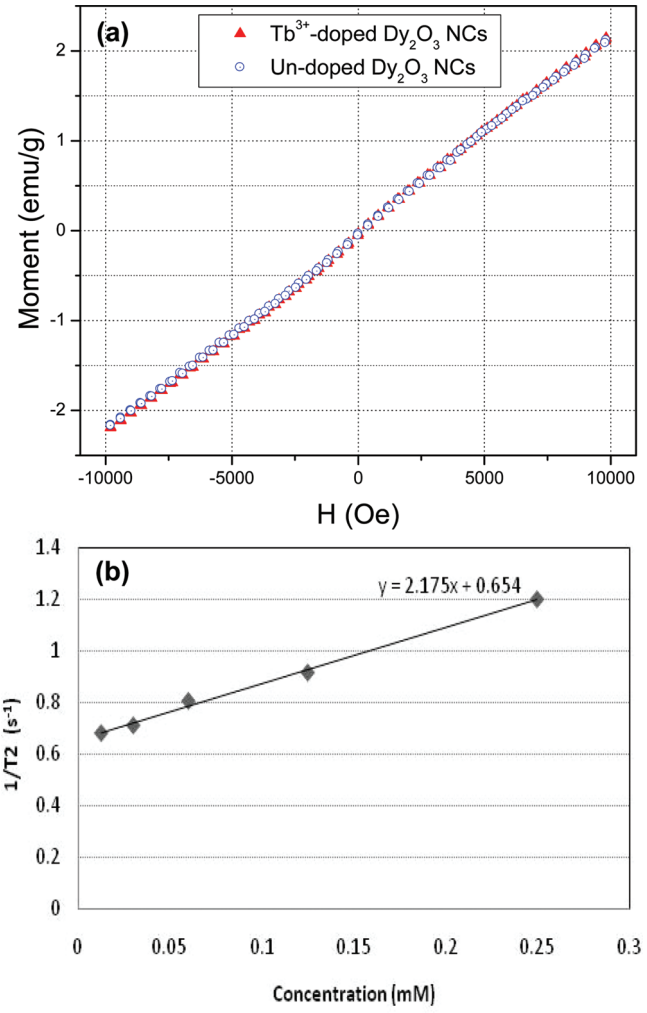

Figure 3. (a) Room temperature magnetization curve of Dy_2O_3:Tb^{3+}NCs. (b)The transverse relaxivity (r_2) plot of Dy_2O_3:Tb^{3+} NCs obtained at various concentrations in 1% agarose gel.

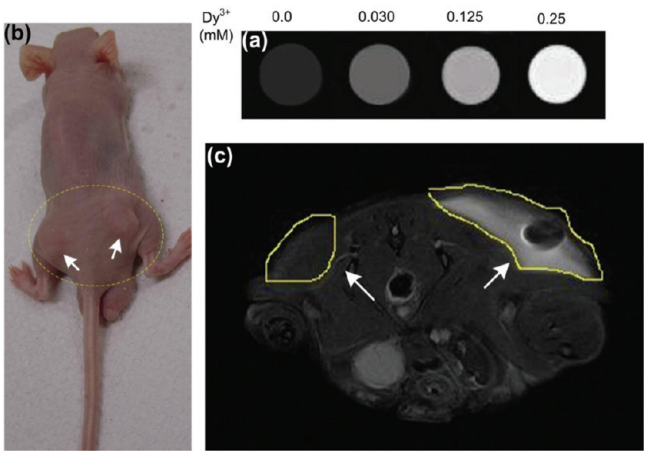

Figure 4. (a) T_2-weighted MR images of silanized Dy_2O_3:Tb^{3+}NCs in 1% agarose gel with increasing concentrations (0, 0.030, 0.125, 0.25 mM) from left to right. (b) Photograph of a nude mouse implanted with breast tumor (MCF-7) cells. The tumor region is marked by a yellow circle while right and left arrows indicate the positions of the two tumors. (c) The in vivo T_2-weighted MR image of tumor regions. The positive contrast arising from Dy_2O_3NCs is clearly seen at the injection site (right arrow) while the tumor (left arrow) serves as a reference, where no NCs were injected.

the left tumor (left arrow) provides a reference where no NCs were injected. It was noticed that the positive contrast arose from a large area surrounding the tumor site. This is because the NCs were not functionalized with tumor targeting moieties and so they accumulated around the neighboring areas. The objective of the current experiment is to demonstrate the in vivo imaging potential of the ultrasmall Dy_2O_3 NCs providing positive contrast for MR imaging. Currently, we are working on the development of suitable strategies to exploit the NCs for in vivo tumor targeting and investigate their biodistribution profile.

Dy^{3+}- based chelates have been reported as T_2 negative contrast agents.[23] Conversely, the current Dy_2O_3NCs show positive contrast in T_2-weighted MRI. Generally, contrast agents including paramagnetic Ln^{3+} ions show both T_1 and T_2 relaxation values but to a different extent. For example, T_1-weighted positive contrast agents demonstrate both T_1 and T_2 relaxation properties, but shortening of longitudinal relaxation (T_1) is dominated over that of transverse relaxation (T_2).[6] This results in the image being brighter within areas where the agents are taken up, due to the brightness being a function of T_1. However, species with high T_1 values lend themselves to darker images. Similarly, T_2-weighted negative contrast influences the signal intensity by shortening transverse relaxation time (T_2), thereby producing darker images while high T_2 results in increased brightness of the image.[6,48] For example, SPIO-based commercially available T_2-weighted negative agents such as Feridex (r_2 = 120 $mM^{-1}s^{-1}$), Resovist (r_2 = 186 $mM^{-1}s^{-1}$) and Combidex (r_2 = 65 $mM^{-1}s^{-1}$), exhibit higher transverse relaxivity (r_2), which implies that these contrast agents have shorter T_2-relaxation time.[7] As a consequence of shorter T_2-relaxation times, these nanomaterials exhibit negative contrast. Other reported T_2-weighted negative contrast agents such as $MnFe_2O_4$ (r_2 = 358 $mM^{-1}s^{-1}$), $CoFe_2O_4$ (r_2 = 172 $mM^{-1}s^{-1}$) and $NiFe_2O_4$ (r_2 = 152 $mM^{-1}s^{-1}$), exhibit similar trend of higher relaxivity (i.e., shorter relaxation time).[7] However, the Dy_2O_3:Tb^{3+} NCs exhibit much smaller transverse relaxivity (r_2 = 2.17 $mM^{-1}s^{-1}$), which indicates that these NCs possess relatively large T_2-relaxation time and hence capable of inducing positive contrast in the phantom and in vivo images. To compare the NC's as-obtained T_2 positive contrast, T_1-weighted phantom images were taken (Supporting Information Figure S2). The relaxivity plot and phantom images of their T_1 MRI suggest that these NCs do not produce significant positive contrast in T_1 MRI. A typical drawback of T_2-weighted negative contrast agents (such as SPIO) is that they offer poor contrast to noise ratio (CNR) in organs such as liver, spleen or in tumors which have inherent low background signal.[49] Considering these aspects, the current T_2-weighted positive contrast agent is advantageous. However, image acquisition time by T_2-weighted positive contrast imaging is usually longer than that of T_1-weighted positive contrast imaging, which can be considered as a potential limitation of this type of contrast agent.

The room temperature photoluminescence (PL) spectra of the Tb^{3+}-doped Dy_2O_3NCs excited at 275 nm is shown in Figure 5a. Four characteristic emission peaks of Tb^{3+} ions appear at 489, 545, 585, and 619 nm from $^5D_4 \rightarrow {}^7F_j$ (j = 6, 5, 4, 3) transitions, respectively.[46] The strongest green emission at 545 nm, corresponding to the $^5D_4 \rightarrow {}^7F_5$ transition, dominates

dx.doi.org/10.1021/cm2003066 |Chem. Mater. 2011, 23, 2439–2446

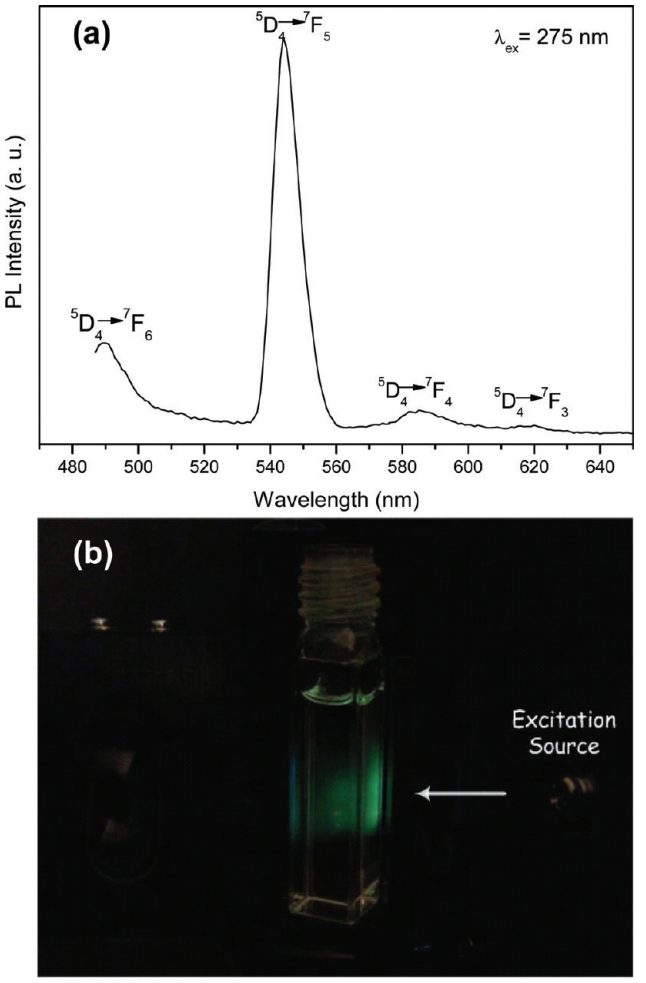

Figure 5. (a) Photoluminescence spectra of Dy_2O_3:Tb^{3+}NCs; (b) Digital photograph of the Dy_2O_3:Tb^{3+} NCs dispersion (~0.1 mg/mL in cyclohexane) showing green emission of the NCs along the path of 275 nm excitation.

over other transitions resulting in green luminescence. A digital photograph (Figure 5b) of the cuvette containing a dispersion of Tb^{3+}-doped Dy_2O_3 NCs (~0.1 mg/mL in cyclohexane) exhibits green emission of the NCs along the path of a 275 nm excitation. It is observed that the intensity of the green emission is reduced to some extent from the near wall to the far wall of the cuvette which is due to the absorption of the incident light by the nanocrystals along its pathway. Tb^{3+}-doped Dy_2O_3NCs were further investigated for fluorescent labeling of live cells. NCs (250 μg/mL) were incubated with human lung epithelial *cells (BEAS-2B)* for 24 h and imaged by confocal microscopy. Confocal fluorescence microscopy images (Figure 6) show that the silanized Tb^{3+}-doped Dy_2O_3NCs were taken up by the living cells and the intracellular concentration of the NCs allowed fluorescent labeling. The NCs were distributed within the cytoplasm, emitting green fluorescence. Heterogeneously distributed fluorescent spots were observed, which is typical of cells exposed to fluorescent nanoparticles. This could be attributed to uneven distribution of NCs across the intracellular regions.[50] Bright field images of the cells after incubation with NCs confirmed that the cells were viable throughout the experiments (Figure 6a). The overlay of bright and dark field images further

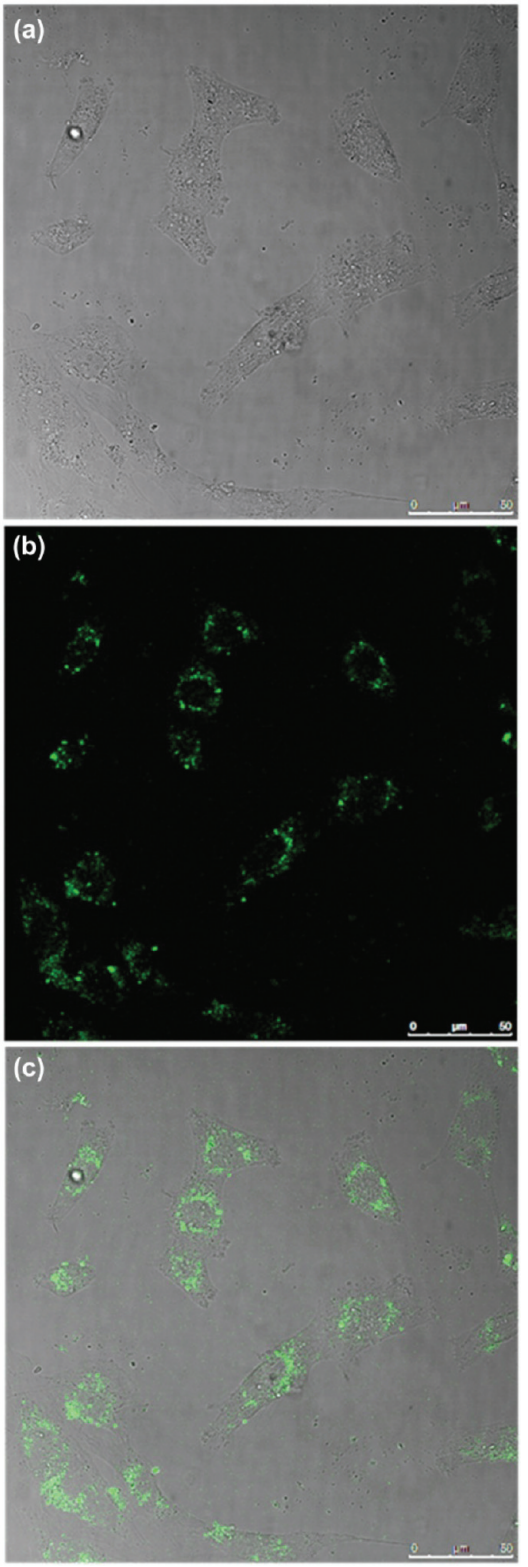

Figure 6. Confocal fluorescent microscopy images of BEAS-2B cells loaded with Dy_2O_3:Tb^{3+} NCs (250 μg/mL) after 24 h incubation. (a) Bright field, (b) Dark field, and (c) The overlaid images show the internalization of the green emitting NCs. Scale bar 50 μm.

demonstrates that the green fluorescence emerged from the intracellular region (Figure 6c), which also suggests that the

dx.doi.org/10.1021/cm2003066 |*Chem. Mater.* 2011, 23, 2439–2446

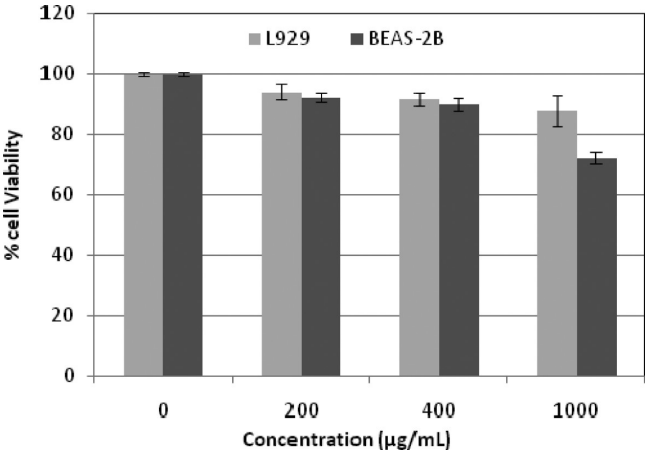

Figure 7. The in vitro cell viability of L929 and BEAS-2B cells incubated with Dy_2O_3:Tb^{3+} NCs with specified concentration upon exposure for 48 h. The error bars indicate the mean square standard deviations.

NCs do not merely stain the membrane surface but are internalized within the cells, with the fluorescent emission originating from different locations across the cell. The results of fluorescence imaging indicate the potential of Dy_2O_3:Tb^{3+}NCs as fluorescent nanoprobes. We are currently pursuing strategies to induce up-conversion fluorescence in Dy^{3+}-type nanomaterials with some compositional modification, since up-conversion fluorescence is more suitable for cell imaging due to its lower phototoxicity.

In vitro cytotoxicity studies were undertaken to investigate the suitability of the NCs as an in vivo contrast agent in MRI and fluorescence imaging. Figure 7 shows the results of the viability test for cells at concentrations ranging from 0 to 1000 μg/mL. Two cells lines, L929 and BEAS-2B, were used to investigate the sensitivity of the nanoparticles toward different cell lines.[36] The highest dosage concentration (i.e., 1000 μg/mL) used in the current cytotoxicity study is similar to that of CdSe quantum dots used by Derfus et al.[51] However, it is higher than most of the reported lanthanide doped nanoparticles studied for cytotoxicity.[36,38,39] The data suggests that the cell viability is greater than 90% for both type of cells after 48 h of exposure, up to NC concentration of 400 μg/mL, which indicates almost negligible toxicity of NCs. However at 1000 μg/mL concentration, the cell viability of BEAS-2B cells was reduced to 72 $\pm$ 2%, while that of L929 remained at 88 $\pm$ 5%. The lower cell viability could be attributed to higher concentration of the NCs being taken up by the cells, leading to cell-death.[36,51,52] The sensitivity of BEAS-2B cells is higher than that of the L929 cells. Hence, the response of different cell types with loaded NCs may differ. In an earlier cell viability experiment with HepG2 and NIH3T3 cells, exposed to either Y_2O_3:Er or Y_2O_3:Yb,Er NCs, we observed that HepG2 is 1.2−1.4 times more resilient than NIH3T3 cells.[36] In BEAS-2B cells, it can be inferred that high concentration of internalized nanoparticles induced generation of additional reactive oxygen species (ROS), which may interrupt ROS and metals ions sequestration.[53] Thus, at high NCs concentration, it is likely that the unsequestered metal ions and ROS remained catalytically active, and increased the inflammatory response of the cells leading to cell death.

4. CONCLUSION

In conclusion, we have developed a facile strategy to synthesize Tb^{3+}-doped Dy_2O_3 NCs that can be utilized as a single-phase bimodal contrast agent for high field (7.0 T) MRI and fluorescence imaging. The T_2-weighted phantom images and in vivo animal imaging have shown high positive contrast. Confocal fluorescence images have displayed the staining of BEAS-2B cells with the NCs. More importantly, the optical and MR properties, and minimal cytotoxicity of the current NCs offer much promise for in vivo targeting and T_2-weighted positive high field MR imaging of organs or regions, which have inherently low background signals.

■ ASSOCIATED CONTENT

Supporting Information. Figures S1 and S2. This material is available free of charge via the Internet at http://pubs.acs.org.

■ AUTHOR INFORMATION

Corresponding Author

*Phone: +65 6316 8822 (T. T. Y. T); +65 6478 8756 (K. K. B). Fax: +65 6794 7553 (T. T. Y. T); +65 6478 8732 (K. K. B). E-mail: tytan@ntu.edu.sg (T. T. Y. T); Kishore_Bhakoo@sbic.a-star.edu.sg (K. K. B).

■ REFERENCES

(1) Cherry, S. R. *Annu. Rev. Biomed. Eng.* **2006**, *8*, 35.
(2) Kim, J.; Piao, Y.; Hyeon, T. *Chem. Soc. Rev.* **2009**, *38*, 372.
(3) Cheon, J.; Lee, J.-H. *Acc. Chem. Res.* **2008**, *41*, 1630.
(4) Baker, M. *Nature* **2010**, *463*, 977.
(5) Weissleder, R.; Pittet, M. J. *Nature* **2008**, *452*, 580.
(6) Bottrill, M.; Kwok, L.; Long, N. J. *Chem. Soc. Rev.* **2006**, *35*, 557.
(7) Na, H. B.; Song, I. C.; Hyeon, T. *Adv. Mater.* **2009**, *21*, 2133.
(8) Selvan, S. T.; Tan, T. T. Y.; Yi, D. K.; Jana, N. R. *Langmuir* **2010**, *26*, 11631.
(9) Jańczewski, D.; Zhang, Y.; Das, G. K.; Yi, D. K.; Padmanabhan, P.; Bhakoo, K. K.; Tan, T. T. Y.; Selvan, S. T. *Microsc. Res. Techniq.* 2010, DOI:10.1002/jemt.20912.
(10) Terreno, E.; Castelli, D. D.; Viale, A.; Aime, S. *Chem. Rev.* **2010**, *110*, 3019.
(11) Chambon, C.; Clement, O.; Le Blanche, A.; Schouman-Claeys, E.; Frija, G. *Magn. Reson. Imaging* **1993**, *11*, 509.
(12) Stuber, M.; Gilson, W. D.; Schär, M.; Kedziorek, D. A.; Hofmann, L. V.; Shah, S.; Vonken, E.-J.; Bulte, J. W. M.; Kraitchman, D. L. *Magn. Reson. Med.* **2007**, *58*, 1072.
(13) Cunningham, C. H.; Arai, T.; Yang, P. C.; McConnell, M. V.; Pauly, J. M.; Conolly, S. M. *Magn. Reson. Med.* **2005**, *53*, 999.
(14) Lipinski, M. J.; Briley-Saebo, K. C.; Mani, V.; Fayad, Z. A. *J. Am. Coll. Cardiol.* **2008**, *52*, 492.
(15) Mani, V.; Briley-Saebo, K. C.; Itskovich, V. V.; Samber, D. D.; Fayad, Z. A. *Magn. Reson. Med.* **2006**, *55*, 126.
(16) Canet, E.; Revel, D.; Forrat, R.; Baldy-Porcher, C.; de Lorgeril, M.; Sebbag, L.; Vallee, J.-P.; Didier, D.; Amiel, M. *Magn. Reson. Imaging* **1993**, *11*, 1139.
(17) Seo, W. S.; Lee, J. H.; Sun, X.; Suzuki, Y.; Mann, D.; Liu, Z.; Terashima, M.; Yang, P. C.; McConnell, M. V.; Nishimura, D. G.; Dai, H. *Nat. Mater.* **2006**, *5*, 971.
(18) Norek, M. g.; Kampert, E.; Zeitler, U.; Peters, J. A. *J. Am. Chem. Soc.* **2008**, *130*, 5335.
(19) Bulte, J. W. M.; Vymazal, J.; Brooks, R. A.; Pierpaoli, C.; Frank, J. A. *Magn. Reson. Imaging* **1993**, *3*, 641.
(20) Gossuin, Y.; Hocq, A.; Vuong, Q. L.; Disch, S.; Hermann, R. e. P.; Gillis, P. *Nanotechnology* **2008**, *19*, 475102.
(21) Viswanathan, S.; Kovacs, Z.; Green, K. N.; Ratnakar, S. J.; Sherry, A. D. *Chem. Rev.* **2010**, *110*, 2960.

(22) Bertini, I.; Capozzi, F.; Luchinat, C.; Nicastro, G.; Xia, Z. *J. Phys. Chem.* **1993**, *97*, 6351.
(23) Elst, L. V.; Roch, A.; Gillis, P.; Laurent, S.; Botteman, F.; Bulte, J. W. M.; Muller, R. N. *Magn. Reson. Med.* **2002**, *47*, 1121.
(24) Kellar, K. E.; Fossheim, S. L.; Koenig, S. H. *Invest. Radiol.* **1998**, *33*, 835.
(25) Bulte, J. W. M.; Wu, C.; Brechbiel, M. W.; Brooks, R. A.; Vymazal, J.; Holla, M.; Frank, J. A. *Invest. Radiol.* **1998**, *33*, 841.
(26) Bridot, J.-L.; Faure, A.-C.; Laurent, S.; Riviere, C.; Billotey, C.; Hiba, B.; Janier, M.; Josserand, V.; Coll, J.-L.; Vander Elst, L.; Muller, R.; Roux, S.; Perriat, P.; Tillement, O. *J. Am. Chem. Soc.* **2007**, *129*, 5076.
(27) Hifumi, H.; Yamaoka, S.; Tanimoto, A.; Akatsu, T.; Shindo, Y.; Honda, A.; Citterio, D.; Oka, K.; Kuribayashi, S.; Suzuki, K. *J. Mater. Chem.* **2009**, *19*, 6393.
(28) Hifumi, H.; Yamaoka, S.; Tanimoto, A.; Citterio, D.; Suzuki, K. *J. Am. Chem. Soc.* **2006**, *128*, 15090.
(29) Das, G. K.; Heng, B. C.; Ng, S.-C.; White, T.; Loo, J. S. C.; D'Silva, L.; Padmanabhan, P.; Bhakoo, K. K.; Selvan, S. T.; Tan, T. T. Y. *Langmuir* **2010**, *26*, 8959.
(30) Happy; Tok, A. I. Y.; Su, L. T.; Boey, F. Y. C.; Ng, S. H. *J. Nanosci. Nanotechnol.* **2007**, *7*, 1.
(31) Nelson, J. A.; Bennett, L. H.; Wagner, M. J. *J. Mater. Chem.* **2003**, *13*, 857.
(32) Wang, F.; Liu, X. *Chem. Soc. Rev.* **2009**, *38*, 976.
(33) Wang, F.; Banerjee, D.; Liu, Y.; Chen, X.; Liu, X. *Analyst* **2010**, *135*, 1839.
(34) Zhang, Y.; Guo, J.; White, T.; Tan, T. T. Y.; Xu, R. *J. Phys. Chem. C* **2007**, *111*, 7893.
(35) Eliseeva, S. V.; Bunzli, J.-C. G. *Chem. Soc. Rev.* **2010**, *39*, 189.
(36) Das, G. K.; Chan, P. P. Y.; Teo, A.; Loo, J. S. C.; Anderson, J. M.; Tan, T. T. Y. *J. Biomed. Mater. Res. Part A* **2010**, *93A*, 337.
(37) Zhang, Y.; Das, G. K.; Xu, R.; Tan, T. T. Y. *J. Mater. Chem.* **2009**, *19*, 3696.
(38) Hu, H.; Xiong, L.; Zhou, J.; Li, F.; Cao, T.; Huang, C. *Chem.—Eur. J.* **2009**, *15*, 3577.
(39) Zhou, J.; Sun, Y.; Du, X.; Xiong, L.; Hu, H.; Li, F. *Biomaterials* **2010**, *31*, 3287.
(40) Lu, H.; Yi, G.; Zhao, S.; Chen, D.; Guo, L.-H.; Cheng, J. *J. Mater. Chem.* **2004**, *14*, 1336.
(41) Selvan, S. T.; Patra, P. K.; Ang, C. Y.; Ying, J. Y. *Angew. Chem., Int. Ed.* **2007**, *46*, 2448.
(42) Kircher, M. F.; Mahmood, U.; King, R. S.; Weissleder, R.; Josephson, L. *Cancer Res.* **2003**, *63*, 8122.
(43) Yi, D. K.; Selvan, S. T.; Lee, S. S.; Papaefthymiou, G. C.; Kundaliya, D.; Ying, J. Y. *J. Am. Chem. Soc.* **2005**, *127*, 4990.
(44) Kim, J.; Lee, J. E.; Lee, S. H.; Yu, J. H.; Lee, J. H.; Park, T. G.; Hyeon, T. *Adv. Mater.* **2008**, *20*, 478.
(45) Shen, J.; Sun, L-D.; Yan, C-H. *Dalton Trans.* **2008**, *42*, 5687.
(46) Das, G. K.; Tan, T. T. Y. *J. Phys. Chem. C* **2008**, *112*, 11211.
(47) Ishiyama, M.; Miyazono, Y.; Sasamoto, K.; Ohkura, Y.; Ueno, K. *Talanta* **1997**, *44*, 1299.
(48) Rinck, P. A. *Magnetic Resonance in Medicine: The Basic Textbook of the European Magnetic Resonance Forum*; Blackwell Scientific Publications: Oxford, 1993.
(49) Corot, C.; Robert, P.; Idée, J.-M.; Port, M. *Adv. Drug Delivery Rev.* **2006**, *58*, 1471.
(50) He, H.; Xie, C.; Ren, J. *Anal. Chem.* **2008**, *80*, 5951.
(51) Derfus, A. M.; Chan, W. C. W.; Bhatia, S. N. *Nano Lett.* **2004**, *4*, 11.
(52) Yin, H.; Too, H. P.; Chow, G. M. *Biomaterials* **2005**, *26*, 5818.
(53) Wang, X.; Wu, Y.; Stonehuerner, J. G.; Dailey, L. A.; Richards, J. D.; Jaspers, I.; Piantadosi, C. A.; Ghio, A. J. *Am. J. Respir. Cell Mol. Biol.* **2006**, *34*, 286.